JACS
JOURNAL OF THE AMERICAN CHEMICAL SOCIETY
pubs.acs.org/JACS
Article

Site-Occupation-Tuned Superionic Li_xScCl_{3+x} Halide Solid Electrolytes for All-Solid-State Batteries

Jianwen Liang,[$] Xiaona Li,[$] Shuo Wang,[$] Keegan R. Adair, Weihan Li, Yang Zhao, Changhong Wang, Yongfeng Hu, Li Zhang, Shangqian Zhao, Shigang Lu, Huan Huang, Ruying Li, Yifei Mo,* and Xueliang Sun*

Cite This: J. Am. Chem. Soc. 2020, 142, 7012−7022

ABSTRACT: The enabling of high energy density of all-solid-state lithium batteries (ASSLBs) requires the development of highly Li^+-conductive solid-state electrolytes (SSEs) with good chemical and electrochemical stability. Recently, halide SSEs based on different material design principles have opened new opportunities for ASSLBs. Here, we discovered a series of Li_xScCl_{3+x} SSEs (x = 2.5, 3, 3.5, and 4) based on the cubic close-packed anion sublattice with room-temperature ionic conductivities up to 3×10^{-3} S cm^{-1}. Owing to the low eutectic temperature between LiCl and $ScCl_3$, Li_xScCl_{3+x} SSEs can be synthesized by a simple co-melting strategy. Preferred orientation is observed for all the samples. The influence of the value of x in Li_xScCl_{3+x} on the structure and Li^+ diffusivity were systematically explored. With increasing x value, higher Li^+, lower vacancy concentration, and less blocking effects from Sc ions are achieved, enabling the ability to tune the Li^+ migration. The electrochemical performance shows that Li_3ScCl_6 possesses a wide electrochemical window of 0.9−4.3 V vs Li^+/Li, stable electrochemical plating/stripping of Li for over 2500 h, as well as good compatibility with $LiCoO_2$. $LiCoO_2/Li_3ScCl_6$/In ASSLB exhibits a reversible capacity of 104.5 mAh g^{-1} with good cycle life retention for 160 cycles. The observed changes in the ionic conductivity and tuning of the site occupations provide an additional approach toward the design of better SSEs.

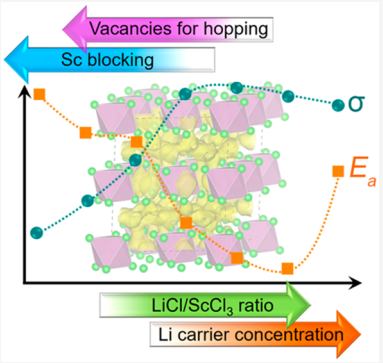

1. INTRODUCTION

All-solid-state lithium batteries (ASSLBs) are more attractive compared to their conventional lithium-ion battery counterparts due to their improved safety, thermal stability, high energy density, and higher voltage compatibility.[1−3] Thus, significant efforts have been made to develop suitable solid-state electrolytes (SSEs) for ASSLBs, such as oxides, polymers, borohydrides, and sulfides. Great research advancements have been made for the aforementioned electrolytes, especially improvements in ionic conductivity approaching 10^{-2} S cm^{-1}.[4−8] Nonetheless, there are still many factors inhibiting their practical application in ASSLBs, such as the high-temperature sintering of oxides, narrow electrochemical windows of polymers and borohydrides, as well as air/moisture hypersensitivity and electrode instability of sulfides.[9−11]

In addition to the above-mentioned SSEs, the recently emerged halide SSEs (such as Li_3YCl_6,[12] Li_3YBr_6,[12] and Li_3InCl_6[13,14]) have proven promising. These SSEs exhibit high ionic conductivities around 10^{-3} S cm^{-1} at room temperature (RT), good compatibility toward oxide cathodes, wide electrochemical windows (for chloride-based electrolytes), and can be synthesized by liquid-phase methods.[14,15] The good compatibility toward oxide cathodes and wide electrochemical windows are highly consistent with simulation results.[16,17] For the cases of fluorides, chlorides, and bromides, the oxidation limit of the electrochemical windows can be as high as >6, 4, and 3 V vs Li^+/Li, respectively.[18] Moreover, the good compatibility toward oxide cathodes should be a general characteristic intrinsic to most of the halide SSEs.[16] On the basis of the tremendous success of recent halide SSEs, it is expected that research in the near future will further reveal the favorable attributes of halide-based systems for ASSLBs. Moreover, different from most of the reported highly conductive SSEs (sulfides, oxide, borohydrides, and metal−organic framework, etc.) where Li^+ migrate through the structural framework built of covalent bonds such as PS_4 tetrahedron, the structures of halide SSEs of Li-M-X (M is metal cation and X is halogen anion) are built by close anion stack based on ionic bonding. Having originated from the essential chemical distinction between the covalent bond and ionic bond, the Li^+ migration through these frameworks will lead to the different phenomenon and diffusion mechanisms.

Received: January 6, 2020
Published: March 26, 2020

https://dx.doi.org/10.1021/jacs.0c00134
J. Am. Chem. Soc. 2020, 142, 7012−7022

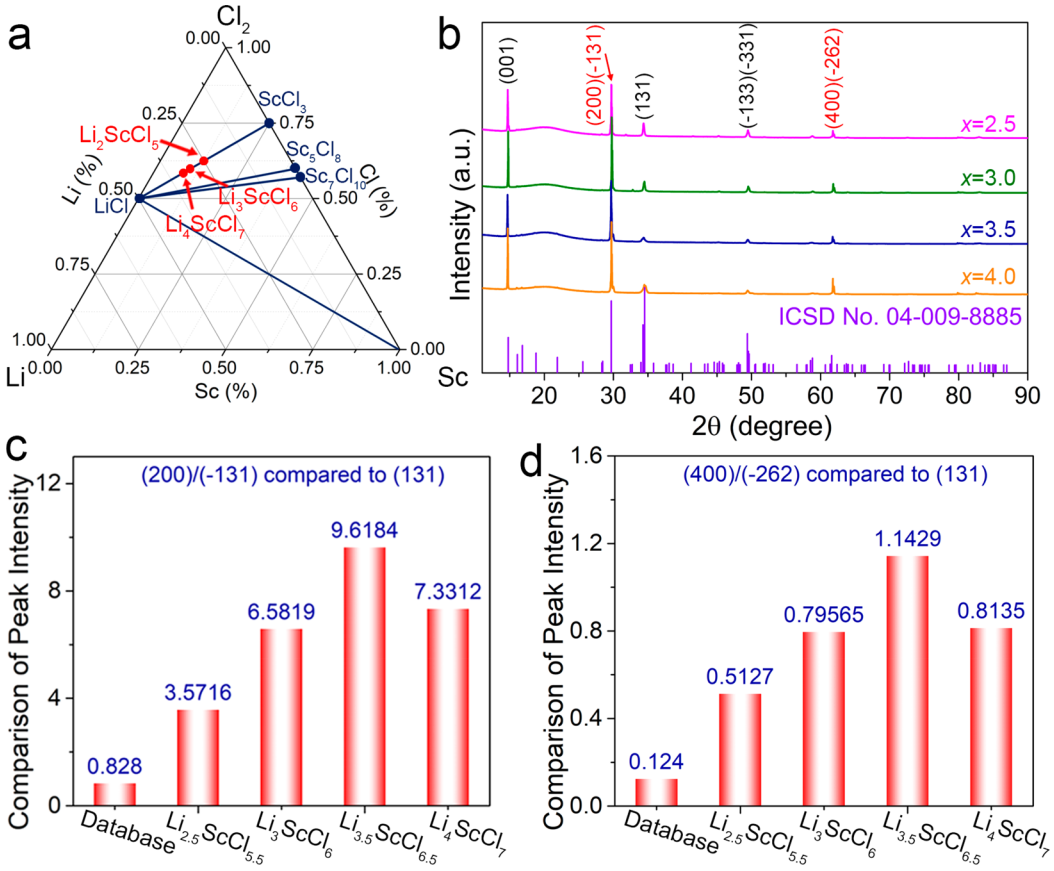

Figure 1. (a) Gibbs triangle of the ternary Li-Sc-Cl composition diagram with formulas of known compounds. The Li_2ScCl_5, Li_3ScCl_6, and Li_4ScCl_7 compounds are highlighted in red. (b) XRD patterns of Li_xScCl_{3+x} SSEs (x = 2.5, 3, 3.5, and 4) SSEs. (c) Peak intensity comparison of (200)/(−131) compared to (131) and (d) peak intensity comparison of (400)/(−262) compared to (131) of Li_xScCl_{3+x} SSEs (x = 2.5, 3, 3.5, and 4) SSEs.

To date, there have only been a few successful examples of halide SSEs that possess high ionic conductivity. Therefore, it is essential to explore other potential halide SSEs to broaden the knowledge and their applications. One of the most critical factors for designing superionic halide SSEs is the structure, which is the dominant factor in determining the ionic conductivities. For example, the reported Li_3YBr_6, Li_3InCl_6, and high-temperature-phase Li_3InBr_6 SSEs with higher ionic conductivity of $1-2 \times 10^{-3}$ S cm^{-1} possess cubic close-packed (ccp)-like anion arrangements with monoclinic structure (space group $C2/m$).[12,14,19,20] Comparatively, the Li_3YCl_6 and Li_3ErCl_6 SSEs, which possess a hexagonal close-packed (hcp)-like anion arrangement with trigonal structure (space group $P\bar{3}m1$) display a relatively lower ionic conductivity of $10^{-5}-10^{-4}$ S cm^{-1}.[12,21,22] Experimentally, halide SSEs with ccp anion sublattices can display high ionic conductivities, though theoretical calculations predict that halide SSEs with hcp anion sublattices may supersede them.[16]

When the developed halide materials were systemically explored, it was found that Li_3MX_6 (M = rare earth metal of La-Lu, Sc, Y; X = Cl, Br) materials with isomorph structures of Li_3InCl_6 and Li_3YBr_6 should be promising halide SSEs. Among the Li_3MX_6 materials, most of the Li_3MBr_6 (M = Sm-Lu)[23] materials also possess ccp anion sublattices with monoclinic structure (space group $C2/m$), which is the same as Li_3YBr_6.[12,23] Meanwhile, the ccp structure can only be formed for the chloride counterpart of Sc-based halide electrolyte-Li_3ScCl_6.[24] In contrast, most of the other chlorides possess hcp anion sublattices with different space groups. For example, Li_3MCl_6 (M = Tb, Dy, Ho, and Er) materials possess a trigonal structure with a $P\bar{3}m1$ space group, and Li_3MCl_6 (M = Yb, Lu) materials possess an orthorhombic structure with a *Pnma* space group.[24−26] Thus, when further taking into consideration the wide electrochemical window of chloride-based SSEs, Li_3ScCl_6 stands out from others due to the potential of simultaneously possessing high ionic conductivity and a wide electrochemical stability window.

Herein, inspired by the possibility of achieving fast Li^+ migration in ccp halide SSEs, we have obtained Li_3ScCl_6 as well as other Li_xScCl_{3+x} SSEs (x = 2.5, 3.5, and 4) that also possess ccp anion sublattices based on a simple co-melting strategy from LiCl and $ScCl_3$. Using Rietveld refinement against X-ray diffraction data and Raman spectroscopy, the structural evolution in Li_xScCl_{3+x} was revealed. It was confirmed that Sc is indeed present in the $ScCl_6^{3-}$ octahedral form with a Sc coordination number of six rather than 4 or 7 coordinated structures, thus only the site occupations within the Li_xScCl_{3+x} were changed. Impedance spectroscopy and first-principle calculations were performed to monitor the changing ionic transport and reveal the diffusion mechanisms. The Li^+ carrier concentration is found to increase with increasing x value in Li_xScCl_{3+x}, while the opposite trend is observed for the total vacancy concentration for hopping and Sc blocking effect within the structure. Thus, the best balance is achieved for Li_3ScCl_6 with appropriate Li^+ carrier concentration and vacancy concentration for Li^+ diffusion in

https://dx.doi.org/10.1021/jacs.0c00134
J. Am. Chem. Soc. 2020, 142, 7012−7022

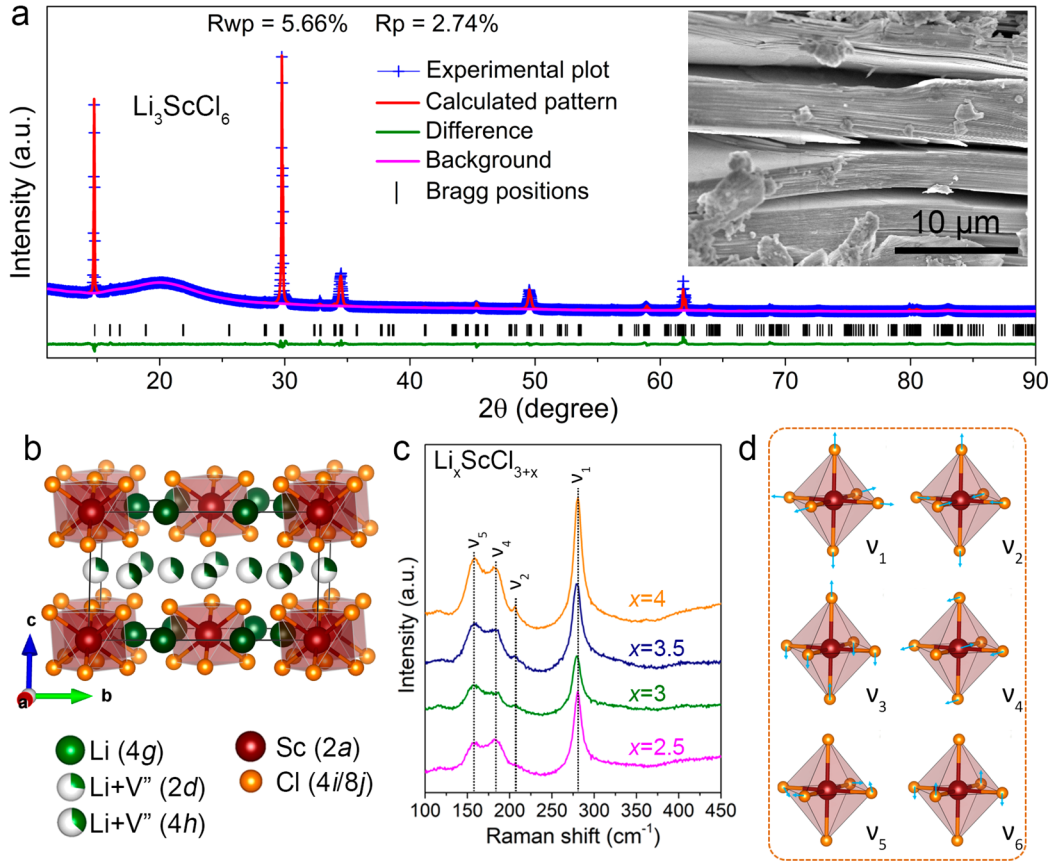

Figure 2. (a) The XRD Rietveld refinement of Li_3ScCl_6 SSE (corresponding SEM image showed insert). (b) Typical crystal structure of Li_3ScCl_6 SSE based on the XRD Rietveld refinement result. (c) Obtained Raman spectra of Li_xScCl_{3+x} SSEs (x = 2.5, 3, 3.5, and 4) showing the typical vibration of $ScCl_6^{3-}$ octahedra. (d) Normal modes of vibrations of $ScCl_6^{3-}$ octahedra.

the continuous ion diffusion channels. As a result, Li_3ScCl_6 possesses the highest RT ionic conductivity (3.02×10^{-3} S cm^{-1}) and a wide electrochemical window of 0.9−4.3 V vs Li^+/Li. Although Li_3ScCl_6 is not stable toward Li in the initial cycles of plating/stripping, a stabilized interface can be gradually formed, ensuring long cycling life over 2500 h for Li/Li_3ScCl_6/Li symmetric cells. Moreover, the remarkable reversibility of the all-solid-state $LiCoO_2$/Li_3ScCl_6/In full cell over 160 cycles was demonstrated. This work reveals fast Li^+ conduction within the Li_xScCl_{3+x} and demonstrates that the local structure, as well as the site occupations of metal/vacancies, affect Li^+ migration in the anion sublattice, which can open up a new route to explore and develop new superionic conductors.

2. RESULTS AND DISCUSSION

The crystal chemistry of the ternary rare-earth halides with general composition $A_aM_bX_{a+3b}$, where A represents monovalent cations, M represents a rare-earth metal, and X represents a halide element, has been well developed. There are different types of $A_aM_bX_{a+3b}$ structures, mainly including AMX_4, A_2MX_5, A_3MX_6, A_4MX_7, and $A_3R_2X_9$. Moreover, the composition of $A_aM_bX_{a+3b}$ in the AX/MX_3 systems is highly dependent on the atomic radii of A^+, M^{3+}, and X^-.[27] Among them, A_3MX_6-type is the most frequently obtained composition (such as Li_3YCl_6/Li_3YBr_6,[12] Li_3InCl_6,[13,14] and Li_3ErCl_6[21,22]). In addition to the existing Li_3ScCl_6, we further investigated other possible stoichiometric ratios of LiCl and $ScCl_3$ within the Li-Sc-Cl Gibbs triangle (Figure 1a). The explored nominal compositions of Li_xScCl_{3+x} are based on the different molar ratios of LiCl and $ScCl_3$, with x values of 1, 1.5, 2, 2.5, 3, 3.5, and 4, respectively.

The Li_xScCl_{3+x} SSEs were synthesized by a co-melting strategy from LiCl and $ScCl_3$ with different molar ratios. When x = 1, 1.5 and 2, though the main X-ray diffraction (XRD) patterns can be indexed to the monoclinic phase, some other obvious peaks can still be observed (Figures S1−S3). Meanwhile, it was found that when $x \geq 2.5$, all the XRD patterns (Figure 1b) can be indexed well with Li_3ScCl_6 ($C2/m$, ICSD No. 04−009−8885, crystallographic data shown in Table S1),[24] which is a monoclinic structure based on a ccp anion arrangement. It should be noted that the XRD patterns of these four samples show strong (001) and (200)/(−131) peaks, indicating a possible preferred orientation. However, the intensity of the (003) peak (around 45.29°) does not show the same trend as the (001) peak. In contrast, the (400)/(−262) peaks also exhibit much stronger intensity compared to that found in the database, demonstrating the preferred orientation along (200)/(−131) of the synthesized samples. As shown in Figure 1c, the peak intensity ratio of (200)/(−131) compared with that of (131) of the Li_xScCl_{3+x} samples ranges from 3.5716 to 9.6184, which is significantly higher than that of 0.828 in the database. The ratio of the peak intensity of (200)/(−131) compared with that of (131) gradually increased along with an increase of x, and reaches the maximum when x = 3.5 followed by a reduction when x = 4. Correspondingly, the peak intensity ratio of (400)/(−262) compared to that of (131) of Li_xScCl_{3+x} samples exhibits the same trend as that presented in

https://dx.doi.org/10.1021/jacs.0c00134
J. Am. Chem. Soc. 2020, 142, 7012−7022

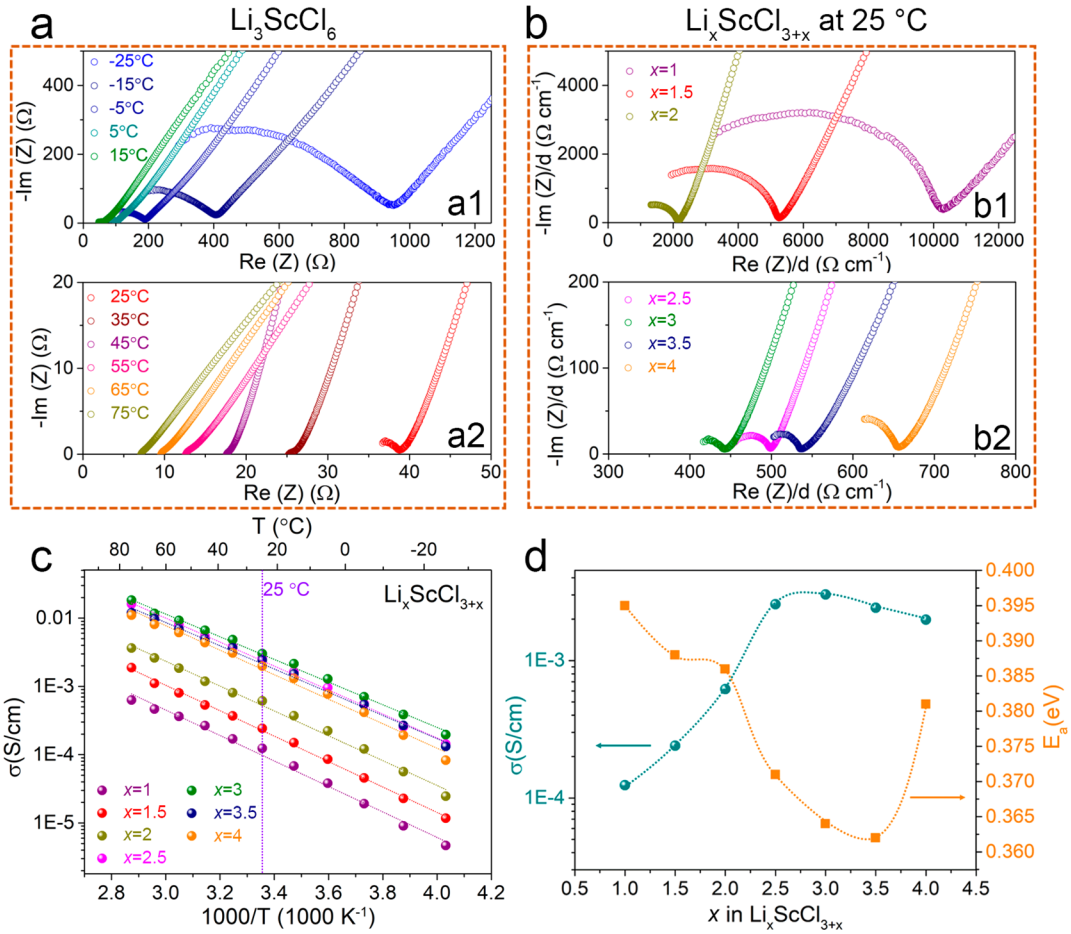

Figure 3. (a) Nyquist plots of Li_3ScCl_6 at different temperatures ranging from −25 to 75 °C. (b) Impedance plots at 25 °C of the cold-pressed pellets of Li_xScCl_{3+x} SSEs (x = 1, 1.5, 2, 2.5, 3, 3.5, and 4) and the impedance is normalized to the respective pellet thickness. (c) Arrhenius conductivity plots of Li_xScCl_{3+x} SSEs (x = 1, 1.5, 2, 2.5, 3, 3.5, and 4). (d) Comparison of RT ionic conductivities and activation energies of Li_xScCl_{3+x} SSEs (x = 1, 1.5, 2, 2.5, 3, 3.5, and 4).

Figure 1d. Another important fact is that the presence of weak peaks is not observed for all the XRD patterns of Li_xScCl_{3+x} ($x \geq 2.5$), which might be caused by system extinction or higher symmetry properties of the as-prepared Li_xScCl_{3+x} samples compared to the monoclinic symmetry in the case of that found in the database.

Representative XRD Rietveld refinement of Li_3ScCl_6 SSE is shown in Figure 2a (detailed structural data are shown in Tables S2 and S3). The typical structure of Li_3ScCl_6 based on the XRD Rietveld refinement result is shown in Figure 2b, which is quite different from that of the reported Li_3YBr_6 and Li_3InCl_6 that can be regarded as distorted LiCl structures.[12,13] The unit cell of Li_3ScCl_6 SSEs contains six crystallographic atom positions (Cl1, Li1, Li2, Li3, Sc1, Cl2). The structure is based on ccp of Cl atoms in the 4*i* and 8*j* sites. Alternate octahedral voids formed by the stacking of Cl atoms are completed and ordered with occupation of Sc and Li atoms along the *c* axis: one layer is fully occupied with Sc1 in the 2*a* site and Li1 in the 4*g* site with the ratio of 1:2 (denoted as Sc +Li layer); the other layer is statistically occupied with Li2 in the 4*h* site and Li3 in the 2*d* site as well as different amounts of partial vacancy (denoted as vacancy+Li layer).[24] Nevertheless, due to the low X-ray form factor for lithium, the detailed results of the lithium position and occupancy can not be obtained accurately. Rietveld refinement results and corresponding structures of other samples can be found in the Supporting Information (Figures S4−S6 and Tables S4−S6). It can be seen that similar to the Li_3ScCl_6, all the Li_xScCl_{3+x} SSEs (x = 2.5, 3.5, and 4) also possess the same structure based on Li−Cl and Sc−Cl octahedral arrangements. The main differences are the occupations of the elements within the structure. For the $Li_{2.5}ScCl_{5.5}$ SSE with a higher content of Sc atoms compared with Li_3ScCl_6, besides the occupation in the pristine Sc+Li layer, partial Sc atoms will also occupy the 4*h* site in the vacancy+Li layer, indicating that Sc atoms occupy each layer of the structure along the *c* axis. For $Li_{3.5}ScCl_{6.5}$ and Li_4ScCl_7 SSEs with lower content of Sc atoms compared with Li_3ScCl_6, Sc vacancies will be formed at the 2*a* site (Sc occupation of 0.98 for $Li_{3.5}ScCl_{6.5}$ and 0.83 for Li_4ScCl_7). The results indicate the high tolerance of the basic structure of typical Li_3ScCl_6, possessing tunable site occupations within the structure, which is a unique characteristic of halide SSEs and should influence the final ionic conductivity to some extent.[28,29] The covalent Sc−Cl orbital mixing and high purity of the Li_xScCl_{3+x} SSEs samples without possible amorphous impurity phase were further confirmed by the Cl K-edge X-ray absorption near-edge structure (XANES) and the corresponding first derivatives shown in Figure S7. The preferred orientation of Li_xScCl_{3+x} SSEs indicated by XRD results was further reflected by the corresponding scanning electron microscopy (SEM) images (insert in Figure 2a and Figures S8−S11), which showed obvious flake-like morphology.

https://dx.doi.org/10.1021/jacs.0c00134
J. Am. Chem. Soc. 2020, 142, 7012−7022

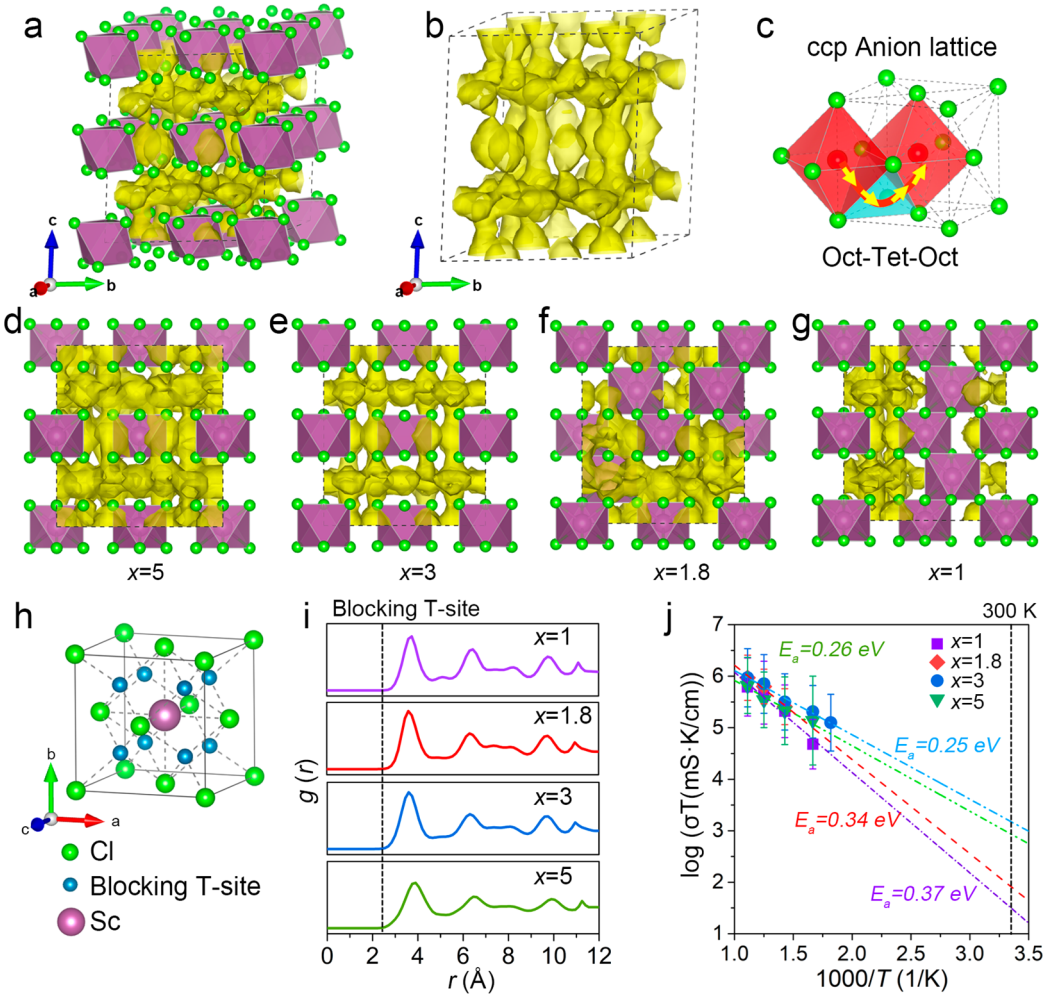

Figure 4. Diffusion mechanism of the Li_xScCl_{3+x} (x = 1, 1.8, 3, and 5) SSEs based on AIMD simulations. (a, b) The Li^+ probability density marked by yellow isosurfaces from AIMD simulations. (c) The Li^+ migration pathways in ccp-anion stacking sublattice of Li_3ScCl_6 structure. The Li^+ probability density marked by yellow isosurfaces of (d) Li_5ScCl_8 (x = 5), (e) Li_3ScCl_6 (x = 3), (f) $Li_{1.8}ScCl_{4.8}$ (x = 1.8) and (g) $LiScCl_4$ (x = 1) structures along a axis. (h) The blocking effect of Sc due to the strong repulsion between Sc and Li. The green, purple, and blue ball represents the Cl, Sc, and blocked tetrahedral site for Li^+ migration, respectively. (i) Radial distribution function (rdf) of Sc−Li ions illustrating the blocking effect of Sc cation in the Li_xScCl_{3+x} (x = 1, 1.8, 3, and 5) SSEs. (j) Arrhenius plot of Li^+ diffusivity in Li_xScCl_{3+x} (x = 1, 1.8, 3, and 5) from AIMD simulations.

Raman spectroscopy was used to further elucidate the structure of Li_xScCl_{3+x} samples. Four typical Raman spectra of Li_xScCl_{3+x} SSEs (x = 2.5, 3, 3.5, and 4) are shown in Figure 2c, presenting the typical vibrational modes of the $ScCl_6^{3-}$ octahedra. Four bands at ∼280, 206, 183, and 158 cm^{-1} were observed for all the spectra, which can be assigned to the ν1, ν2, ν4, and ν5 vibrational modes (Figure 2d) of $ScCl_6^{3-}$ octahedra.[30,31] No other signals for possible $ScCl_4^-$ (310 cm^{-1}) and $ScCl_7^{4-}$ (260 cm^{-1}) species are found,[30,31] demonstrating that there are no four-coordinated species ($ScCl_4^-$) or seven-coordinated species ($ScCl_7^{4-}$) for all the Li_xScCl_{3+x} SSEs (x = 2.5, 3, 3.5, and 4), even for the stoichiometric Li_4ScCl_7 compound. The Raman results are in accordance with the XRD Rietveld refinement results shown in Figure 2a,b and Figures S4−S6. Moreover, all the Li_xScCl_{3+x} SSEs (x = 2.5, 3, 3.5, and 4) possess the basic $ScCl_6^{3-}$ octahedral arrangement with Sc coordination number of six. The results are also consistent with the previous reports about $A_aM_bX_{a+3b}$ halide materials.[27] The lack of $ScCl_7^{4-}$ is due to the small Sc^{3+} radius of 74.5 pm compared to 181 pm for Cl^-, and until now, the $LiMCl_4$-type compounds were only found for M = Sm−Gd.[27] The obtained Li_xScCl_{3+x} SSEs (x = 2.5, 3, 3.5, and 4) were found to have a similar ccp anion sublattice structure with the same basic $ScCl_6^{3-}$ octahedral arrangement (Sc coordination number of six), even in the case of the stoichiometric Li_4ScCl_7 compound. Thus, the highly tunable structure of halide SSEs is demonstrated.

The Li^+ conductivity of Li_xScCl_{3+x} was determined by impedance measurements at different temperatures in a blocking electrode configuration. Impedance spectra of typical Li_3ScCl_6 SSE at different temperatures are presented in Figure 3a, showing a semicircle at high frequency and a tail at low frequency. The impedance spectra were fit with an equivalent circuit consisting of one parallel constant phase element (CPE)/resistor (R) in series with another CPE, where R includes both intragrain and grain boundary contributions within the SSE. The CPE/R exceeded the range of the impedance analyzer at a higher temperature (Figure 3a2), thus only the tail of the blocking electrodes was used during fitting. Impedance plots of all the Li_xScCl_{3+x} SSEs (x = 1, 1.5, 2, 2.5, 3, 3.5, and 4) at 25 °C are shown in Figure 3b. Li_3ScCl_6 SSE exhibits the highest ionic conductivity of 3.02×10^{-3} S cm^{-1}

https://dx.doi.org/10.1021/jacs.0c00134
J. Am. Chem. Soc. 2020, 142, 7012−7022

based on the equation of σ = d/RS, where d and S are the thickness and the cross-sectional area of the pellets, respectively. Arrhenius conductivity plots of Li_xScCl_{3+x} SSEs based on the impedance spectra at different temperatures of all the samples were further compared in Figure 3c, and the resultant RT ionic conductivities and activation energies (E_a) of all the samples are summarized in Figure 3d and Table S7.

The relatively low ionic conductivity of $LiScCl_4$ and $Li_{1.5}ScCl_{4.5}$ SSEs ($1.23-2.42 \times 10^{-4}$ S cm^{-1}) also leads to relatively high E_a values as presented in Figure 3d. However, all the other Li_xScCl_{3+x} SSEs (x = 2.5, 3, 3.5, and 4) display faster Li^+ migration ranging from 1.98×10^{-3} to 3.02×10^{-3} S cm^{-1}, which are the best among the reported halide SSEs.[12−14,21,22] More importantly, the structure of the as-synthesized Li_xScCl_{3+x} SSEs (with high ionic conductivity over 10^{-3} S cm^{-1}) consists of a ccp anion sublattice, which is different from that of Li_3ScCl_6 with the hcp anion sublattice that has been previously reported based on theoretical results.[16] Indeed, as confirmed by the XRD Rietveld refinement and Raman results, all the Li_xScCl_{3+x} SSEs (x = 2.5, 3, 3.5, and 4) possess a similar monoclinic structure (ccp sublattice) of Li_3ScCl_6 with configurational variability of Sc and Cl site occupations in the octahedral lattice. Correspondingly, the total vacancy content within the Li_xScCl_{3+x} SSEs is also adjusted by the x value, with higher vacancy content achieved along with a decrease of x (i. e., Li^+ concentration). As evidenced by the impedance test, Li_3ScCl_6 showed the highest RT ionic conductivity among Li_xScCl_{3+x} SSEs, though it only possesses Li vacancy within the structure. Thus, there should be a balance between Li^+ concentration and total vacancy content that dominates the final ionic conductivity. The typical electronic conductivity of Li_3ScCl_6 SSE determined by direct current (DC) polarization measurements in the range from 100 to 500 mV is about 2.92×10^{-9} S cm^{-1} (Figure S12), which can be regarded as almost insulating electron transport compared to the fast Li^+ migration. Furthermore, the Li_3ScCl_6 SSE also exhibits good dry-air and temperature stability reflected by the thermogravimetric analysis (TGA) test (Figure S13).

Moreover, first-principles calculations were performed to further reveal the diffusion mechanism in these new halide SSEs as a result of different configurations and site occupation of Sc and Li cations. All the calculations were carried out using the Vienna Ab initio Simulation Package (VASP)[32] based on density functional theory (DFT). The projector augmented-wave[33] (PAW) approach and Generalized gradient approximation (GGA) with the Perdew−Burke−Ernzerhof (PBE) functional[34] were used for the energy calculations, structural optimization, and ab initio molecular dynamics (AIMD) simulations. The plane-wave energy cutoff and k-points density used in the calculations were consistent with those of the Materials Project.[35] The detailed information about the calculation can be found in the Supporting Information. In all Li_xScCl_{3+x} compounds with different occupations, stable Li and Sc positions are located at the octahedral sites of a Cl ccp-anion stacking sublattice. On the basis of the structures and site occupations from XRD refinement results, all symmetrically distinctive structures in a primitive cell were generated for the Li_xScCl_{3+x} (x = 1, 3) and 20 symmetrically distinctive structures were generated by minimizing the electrostatic energies from 1000 random configurations for the Li_xScCl_{3+x} (x = 1.8, 5) in a 2 × 1 × 2 supercell using the *pymatgen* package[36] as in previous work.[37,38] Then, all these structures were structurally relaxed in the DFT calculations, and the structure with the lowest energy was identified as the ground state structure for other calculations. Table S8 and Figure S14 summarize all of these model structures and the related energies above the convex hull (ΔE_{hull}). Li_3ScCl_6 possesses the lowest hull energy about 17 meV/atom, indicating good phase stability. We performed the AIMD simulations to investigate the Li^+ diffusion in the Li_3ScCl_6 structure. The Li^+ probability density from AIMD simulation was marked as yellow iso-surfaces which illustrate the 3D Li^+ diffusive channels (Figure 4a,b). As observed in AIMD simulations, the lithium-ion hops from one octahedral site to a neighboring octahedral site through a tetrahedral interstitial site (Oct-Tet-Oct, Figure 4c), forming a three-direction isotropic diffusion network (Figure 4b). For comparison, the Li^+ migration pathways of other structural models based on x = 1, 1.8, and 5 exhibit notable differences in Li^+ migration (Figure 4d−g). As mentioned above, there are two different positive ionic layers along the c axis, i.e., the Sc+Li (2*a* and 4*g* sites) layer and the vacancy+Li (4*h* and 2*d* sites) layer. When x is higher than 3, the occupation of Sc1 in 2*a* decreases along with increased occupancy of Li in 4*h* and 2*d* sites, leading to an increased Li^+ concentration but decreased vacancies for lithium diffusion. The pathway of lithium ions in Li_5ScCl_8 (Figure 4d) is similar to Li_3ScCl_6 (Figure 4e). When x is lower than 3, more introduced Sc ions occupy the position of Li2 or Li3 sites in the vacancy+Li layer. Due to the repulsive Coulombic interaction between Sc^{3+} and Li^+, the tetrahedral interstitial sites adjacent to Sc^{3+} are blocked, which is shown as blue sites in Figure 4h. This blocking effect is further confirmed in the Li−Sc radial distribution function in AIMD simulations for all Li_xScCl_{3+x}, as no peak exists at the tetrahedral site (i.e., blocking site) neighboring the Sc site at ∼2.3 Å, which is consistent with the absence of Li^+ probability around Sc^{3+} in Figure 4d−g and Figures S15−S18. This explains the different Li^+ migration pathways in $Li_{1.8}ScCl_{4.8}$ (Figure 4f) and $LiScCl_4$ (Figure 4g) compared with those of Li_3ScCl_6. Since partial Li^+ migration pathways are blocked, the Li^+ migration energy barrier may increase, which is consistent with the experimental results shown in Figure 3. Furthermore, the rates of effective ion hops from AIMD simulations were calculated (Figure S19); the effective rates of the ionic hopping for $LiScCl_4$ (x = 1), $Li_{1.8}ScCl_{4.8}$ (x = 1.8), Li_3ScCl_6 (x = 3), and Li_5ScCl_8 (x = 5) are 1.3, 1.1, 1.6, and 1.0 times per picosecond at 700 K, respectively. Li_3ScCl_6 also exhibits the highest rate of the ionic hopping. As a result, the Li_3ScCl_6 structure achieves the optimal vacancy concentration for Li^+ conduction and continuous network of diffusion channels. The ionic conductivities and activation energies of the four structures based on AIMD simulation were compared in Figure 4j and Table S9. The ionic conductivities of $LiScCl_4$ (x = 1), $Li_{1.8}ScCl_{4.8}$ (x = 1.8), Li_3ScCl_6 (x = 3), and Li_5ScCl_8 (x = 5) at 300 K are 0.18, 0.44, 5.1, and 2.4 mS cm^{-1}, respectively, showing the same trend of experimental results (Figure 3 and Table S7). The Haven ratio for these compositions is close to 1 (Table S10), which suggests most of the ion hoppings are uncorrelated. The calculated E_a of 0.25 ± 0.04 eV for Li_3ScCl_6 is similar to that of Li_5ScCl_8 (0.26 ± 0.07 eV), while the ionic conductivity of Li_5ScCl_8 is lower than that of Li_3ScCl_6. This originates from the low rate of the ionic hopping in Li_5ScCl_8 due to the low concentration of vacancies in the structure. The calculated E_a values of $LiScCl_4$ (0.37 ± 0.07 eV) and $Li_{1.8}ScCl_{4.8}$ (0.34 ± 0.07 eV) are higher than that of Li_3ScCl_6,

https://dx.doi.org/10.1021/jacs.0c00134
J. Am. Chem. Soc. 2020, 142, 7012−7022

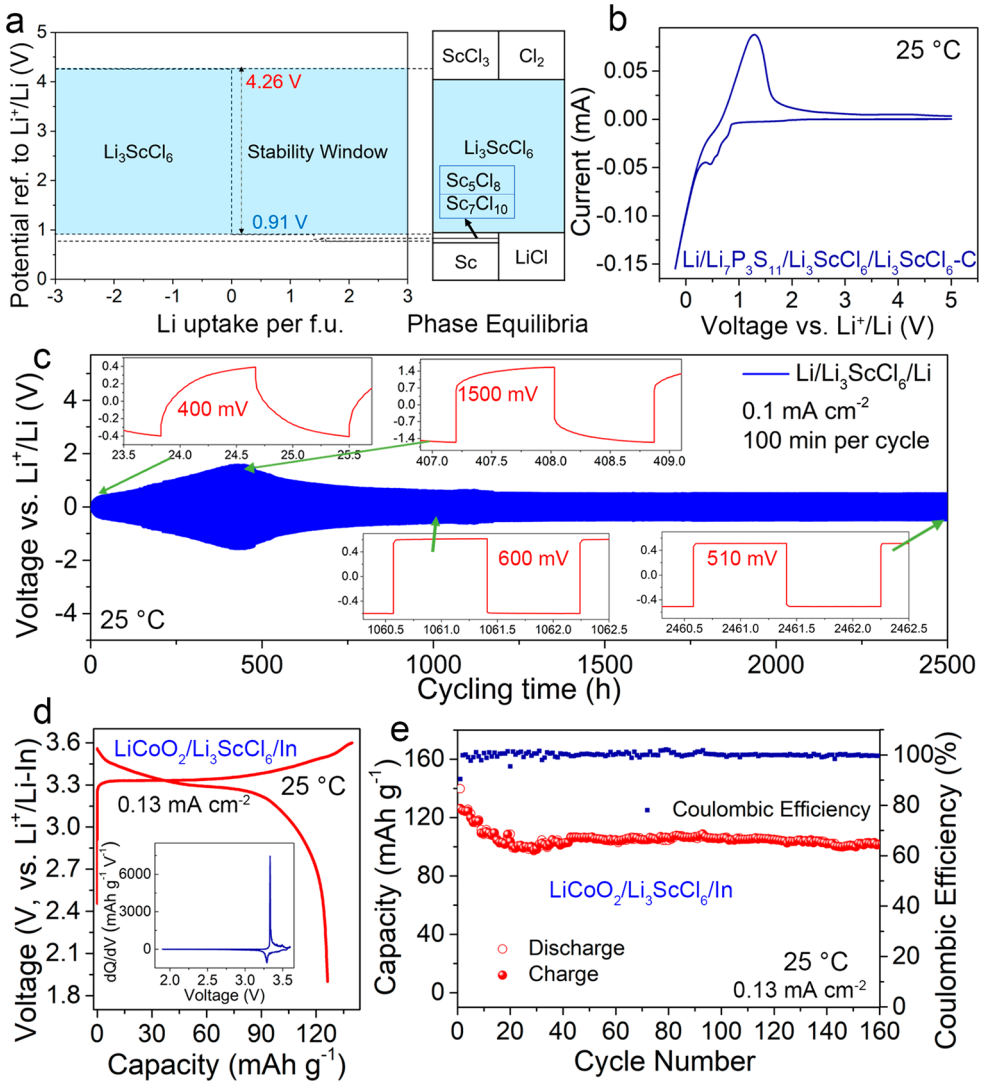

Figure 5. Electrochemical performance of Li_3ScCl_6 SSE at 25 °C. (a) Thermodynamic equilibrium voltage profile and the phase equilibria for Li_3ScCl_6 based on first-principle calculations. (b) CV curves of all-solid-state $Li/Li_7P_3S_{11}/Li_3ScCl_6/Li_3ScCl_6$–C cell at 0.1 mV s^{-1} (Li_3ScCl_6 and carbon mass ratio of 5:5). (c) Electrochemical performance of the symmetric all-solid-state $Li/Li_3ScCl_6/Li$ cell at 0.1 mA cm^{-2} (100 min per plating/stripping cycle). (d) Initial charge/discharge curves of all-solid-state $LiCoO_2/Li_3ScCl_6/In$ cell at 0.13 mA cm^{-2} at room temperature (corresponding dQ/dV curves shown insert). (e) Cycling stability and coulombic efficiency of all-solid-state $LiCoO_2/Li_3ScCl_6/In$ cell at 0.13 mA cm^{-2}.

which is due to the blocking effect of extra Sc occupation in the vacancy+Li layer. On the basis of the variable site occupation configurations within Li_xScCl_{3+x} SSEs, it was proven that the Sc blocking effect, Li^+ carrier concentration, and vacancy concentration for hopping are the three key parameters to determine the Li^+ diffusion. The best balance can be obtained with appropriate vacancy concentration for Li^+ diffusion and continuous diffusive channels. The observed change of Li^+ diffusion mechanism in halide SSEs with site occupation tuning has not been observed from other highly conducting SSEs where Li^+ migration occurs through well-formed channels of the crystal structural frameworks.[39] These findings indicate that the material design principles, especially regarding the local structure change and element/vacancy distribution in the structure, are critical in understanding and developing the halide SSEs.

Besides the ionic conductivity, the thermodynamic intrinsic electrochemically stable window of Li_3ScCl_6 SSE was calculated by using the established scheme[40−42] based on the Materials Project[35] database. The equilibrium voltage profile and corresponding phase equilibria as a function of applied potential referenced to Li^+/Li are shown in Figure 5a and Table S11. For Li_3ScCl_6 SSE, the electrochemical oxidation process originates from the Cl^- anion chemistry with products such as $ScCl_3$ and Cl_2. The electrochemical reduction process is mainly caused by the Sc^{3+} cation chemistry, resulting in LiCl and Sc−Cl compounds with different Sc/Cl ratios such as Sc_5Cl_8 and Sc_7Cl_{10} followed by reduction to Sc metal. The Li_3ScCl_6 SSE shows a wide electrochemical window with an anodic limit of 4.26 V (vs Li^+/Li) and a cathodic limit of 0.91 V (vs Li^+/Li). The thermodynamic window is significantly wider than those of many current SSEs, especially for the electrolytes with ionic conductivities higher than 1 mS cm^{-1} such as Li_6PS_5Cl (1.71−2.14),[40] LGPS (1.72−2.42 V),[43] $Li_{0.33}La_{0.56}TiO_3$ (1.75−3.71 V),[43] LISICON (1.44−3.39 V),[40] Li_3OCl (0−2.55 V),[44] Li_3YBr_6 (0.59−3.15),[16] and Li_3InCl_6 (2.38−4.3 V).[16]

https://dx.doi.org/10.1021/jacs.0c00134
J. Am. Chem. Soc. 2020, 142, 7012−7022

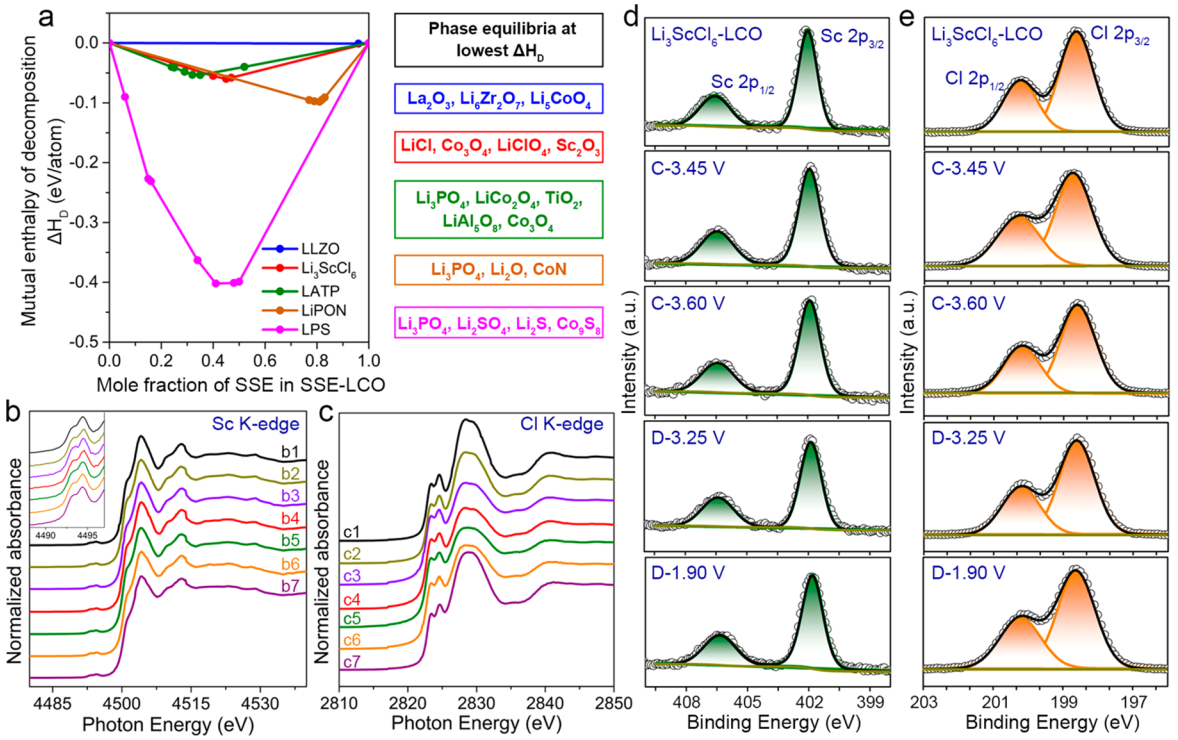

Figure 6. Compatibility between Li_3ScCl_6 SSE and $LiCoO_2$. (a) Calculated mutual reaction enthalpy between SSE and $LiCoO_2$ as a function of mixing ratio and the corresponding phase equilibria (in box) at the lowest point along the energy convex hull. *Ex-situ* (b) Sc K-edge and (c) Cl K-edge XANES spectra of Li_3ScCl_6-$LiCoO_2$ (Li_3ScCl_6-LCO) cathode composites at different charge−discharge states, i.e., (b1, c1) pristine Li_3ScCl_6-LCO, (b2, c2) charged to 3.35 V, (b3, c3) charged to 3.45 V, (b4, c4) fully charged to 3.60 V, (b5, c5) discharged to 3.35 V, (b6, c6) fully discharged to 1.90 V, and (b7, c7) fully discharged to 1.90 V after 50 cycles. *Ex-situ* (d) Sc 2p and (e) Cl 2p XPS spectra of Li_3ScCl_6-LCO cathode composites at different charge−discharge states, i.e., pristine Li_3ScCl_6-LCO, charged to 3.45 V, fully charged to 3.60 V, discharged to 3.25 V, fully discharged to 1.90 V. All the charge/discharge voltages versus Li^+/LiIn here.

Cyclic voltammetry (CV) testing of all-solid-state Li/Li_3ScCl_6/Li_3ScCl_6+C and Li/$Li_7P_3S_{11}$/Li_3ScCl_6/Li_3ScCl_6−C cells at 0.1 mV s^{-1}, in which Li_3ScCl_6 was mixed with 50 wt % carbon to improve the electron conduction, was further performed to evaluate its actual electrochemical stability window.[45−47] As presented in Figure S20, two obvious reduction peaks at 0.53 and 0.15 V, as well as one oxidation peak at 4.08 V (with oxidation onset of 3.72 V), are identified in the cell configuration of Li/Li_3ScCl_6/Li_3ScCl_6+C. However, it should be noted that the oxidation voltage reflected here is not fixed at Li^+/Li redox potential since the reference electrode potential was changed due to the reaction between Li_3ScCl_6 SSE and Li metal. Thus, a layer of commercial $Li_7P_3S_{11}$ was inserted between Li_3ScCl_6 SSE and bare Li metal to fix the reference electrode potential. The CV curve of Li/$Li_7P_3S_{11}$/Li_3ScCl_6/Li_3ScCl_6−C cell in Figure 5b shows slightly different reduction/oxidation behavior compared to the cell without $Li_7P_3S_{11}$ protection layer, in which there are two reduction peaks at 0.75 and 0.5 V and no obvious oxidation peak up to 5.0 V. The experimentally measured electrochemical stability window of Li_3ScCl_6 SSE is diverged from that of 0.91−4.26 vs Li^+/Li as theoretically calculated, which can be attributed to the polarization as well as the interface formation during CV testing. To evaluate the anodic stability, symmetric all-solid-state Li cells using Li_3ScCl_6 as the electrolyte were further constructed. The charge/discharge profiles of Li/Li_3ScCl_6/Li at 0.1 mA cm^{-2} with 100 min per cycle are shown in Figure 5c. Initially, Li plating/stripping occurred at around ±400 mV, then gradually increased to ±1500 mV (~400 h), and finally decreased to ±510 mV over 2500 h. The initial increase of plating/stripping potentials should be caused by the severe interfacial reaction between Li and Li_3ScCl_6 SSE, and the decrease of the plating/stripping voltage in subsequent cycles might be due to the gradual formation of a stable interface as well as a higher contact area between active Li and SSE. The electrochemical impedance spectra (EIS) evolution of the Li/Li_3ScCl_6/Li cell recorded at different aging times and cycle numbers presented in Figures S21 and S22 also showed the formation of a gradually stabilized interface, as reflected by the almost unchanged interfacial resistance after a certain period of time during the plating/stripping process. The same trend was also observed for the Li/Li_3ScCl_6/Li cell at a higher capacity of 0.5 mAh cm^{-2} as presented in Figure S23, with a steady overpotential of ±620 mV over 2800 h. To the best of our knowledge, this is the first time to report a Li-M-Cl (M is a metal element) halide SSE that can be cycled directly against bare Li metal although it still reveals a high polarization voltage. On the basis of this, suitable Li protection strategies might be able to reduce this high polarization voltage and provide improved Li symmetric cell performances.

The high oxidation stability of Li_3ScCl_6 at >4.2 V supports the use of current commercial 4 V-class cathode materials such as $LiCoO_2$ in ASSLBs. Thus, the as-synthesized Li_3ScCl_6 is further evaluated in ASSLBs using indium (In) as the anode and $LiCoO_2$ as the cathode at 25 °C. Similar to other halide SSEs, Li_3ScCl_6 was directly hand-milled with bare $LiCoO_2$ to fabricate cathode composites (mass ratio of Li_3ScCl_6:$LiCoO_2$ of 3:7) without any protective coating layers for $LiCoO_2$. The EIS evolution at steady state over 24 h is presented in Figure S24 and indicates the stability of the electrolyte/electrode

https://dx.doi.org/10.1021/jacs.0c00134
J. Am. Chem. Soc. 2020, 142, 7012−7022

interfaces in the $LiCoO_2/Li_3ScCl_6$/In full cell. Figure 5d shows the initial charge/discharge voltage profiles of the $LiCoO_2/Li_3ScCl_6$/In cell at 0.13 mA cm^{-2} ($LiCoO_2$ loading of 8.92 mg cm^{-2}). The $LiCoO_2/Li_3ScCl_6$/In cell shows an initial charge capacity of 139.7 mAh g^{-1} and a discharge capacity of 126.2 mAh g^{-1}, corresponding to an initial Coulombic efficiency of 90.3%. Typical redox reaction peak associated with cobalt can be clearly observed in the dQ/dV curves (insert in Figure 5d). Figure 5e displays the cycling performance of the $LiCoO_2/Li_3ScCl_6$/In full cell at 0.13 mA cm^{-2}. After the slight decrease in the initial several cycles, the $LiCoO_2/Li_3ScCl_6$/In full cell displays stable cycling with a capacity of 104.5 mAh g^{-1} maintained as well as a high Coulombic efficiency of 99.2% after 160 cycles.

Compared to sulfide and oxide SSEs, on the cathode side, Li_3ScCl_6 SSE reveals a significant advantage in compatibility toward oxide cathodes without any interfacial modification. Typically, the side reactions and interface formation between the SSE and cathode material are critical factors affecting the performance of ASSLBs. The possible interfacial component between Li_3ScCl_6 and $LiCoO_2$ using the pseudobinary model was calculated and shown in Figure 6a and Table S12, the calculation of some other common SSEs was also presented as a comparison. The reaction energy of Li_3ScCl_6 with the $LiCoO_2$ cathode is around 60 meV/atom, which is 1 order of magnitude less than that of sulfide SSEs and half of that of LiPON SSEs, suggesting good interfacial stability between $LiCoO_2$ and Li_3ScCl_6 SSEs (Table S12). Moreover, the Li_3ScCl_6 electrolyte remains compatible with delithiated $Li_{0.5}CoO_2$, with an even smaller reaction energy of 35 meV/atom. Thus, the good interfacial stability between Li_3ScCl_6 and the $LiCoO_2$ cathode during electrochemical cycling is revealed, which is consistent with the high Coulombic Efficiency (90.3%) as well as the stable cycling of $LiCoO_2/Li_3ScCl_6$/In cell.

The compatibility of the Li_3ScCl_6 toward $LiCoO_2$ cathode was further proved through use of XANES and X-ray photoelectron spectroscopy (XPS) analysis (Figure 6b–e). The collected Sc and Cl K-edge XANES spectra of the Li_3ScCl_6–$LiCoO_2$ cathode composite and those at different charge/discharge states are presented in Figure 6b,c. For the Sc K-edge spectra, all samples display a split pre-edge feature (peak splitting about 1.5 eV, insert in Figure 6b) due to the 1s → 3d (t_{2g} and e_g) transition, demonstrating the octahedral environment of Sc atoms. The other pronounced feature of >4503 eV corresponds to the main edge resonance of the E_1 transitions toward the empty 4p state of the Sc atoms (1s → 4p).[48,49] For the Cl K-edge spectra, two well-resolved pre-edge features at 2823.4 eV (1s → t_{2g}) and 2824.7 eV (1s → e_g) that are indicative of covalent Sc–Cl orbital mixing were observed.[50] Overall, the Sc and Cl K-edge XANES spectra of all the samples are quite similar without obvious change, demonstrating the good compatibility between Li_3ScCl_6 and $LiCoO_2$ cathode during cycling. Moreover, the first derivatives of the Sc and Cl K-edge XANES spectra (Figure S25,26) further support this conclusion. Furthermore, the Sc 2p and Cl 2p XPS spectra of Li_3ScCl_6–$LiCoO_2$ cathode composites at different charge/discharge states (Figure 6d,e) also showed no obvious change of peak position. Combined with the theoretical calculations, *ex-situ* XANES, and *ex-situ* XPS, the good stability of Li_3ScCl_6 SSE toward $LiCoO_2$ (as well as $Li_{0.5}CoO_2$ in a delithiated state) and the stability of Li_3ScCl_6 SSE itself within the applied voltage range can be concluded.

3. CONCLUSIONS

In summary, tuning of the local structure as well as the site-occupation of Sc/vacancies in Li_xScCl_{3+x} SSEs (x = 2.5, 3, 3.5, and 4) was successfully demonstrated by a simple co-melting synthesis strategy. XRD and SEM results indicate the Li_xScCl_{3+x} SSEs have a highly preferred structural orientation. Complementary analysis by XRD Rietveld refinement and Raman measurements reveal the same basic $ScCl_6^{3-}$ octahedral arrangement with Sc coordination number of six for Li_xScCl_{3+x}, even for the first reported stoichiometric Li_4ScCl_7 compound. The variability of site occupation configurations, vacancy content in the octahedral lattice, and Li^+ diffusion mechanism upon changing the Li concentration in Li_xScCl_{3+x} SSEs is also illuminated. The Li_xScCl_{3+x} SSEs showed high RT ionic conductivity over 10^{-3} S cm^{-1}, with the highest value of 3.02×10^{-3} S cm^{-1} achieved for Li_3ScCl_6 through balancing of the Li^+ carrier and vacancy for hopping concentrations that get rid of the Sc blocking effect. Our study further highlights the good electrochemical stability of these SSEs. Typical Li_3ScCl_6 showed a significantly wide electrochemical window, a good compatibility with bare $LiCoO_2$, and gradually increased stability toward Li during the plating/stripping process. Our findings demonstrate that Li_xScCl_{3+x} are promising SSEs for ASSLBs; the structures of halide SSEs are highly tunable; and the Li^+ diffusivity of halide SSEs can be adjusted by tuning the site occupations within the structure.

■ ASSOCIATED CONTENT

Supporting Information

The Supporting Information is available free of charge at https://pubs.acs.org/doi/10.1021/jacs.0c00134.

Complete experimental details, electrochemical/interface stability calculation, ab initio molecular dynamics simulations (PDF)

■ AUTHOR INFORMATION

Corresponding Authors

Xueliang Sun − *Department of Mechanical and Materials Engineering, University of Western Ontario, London, Ontario N6A 3K7, Canada;* orcid.org/0000-0003-0374-1245; Email: xsun9@uwo.ca

Yifei Mo − *Department of Materials Science and Engineering, University of Maryland, College Park, Maryland 20742, United States;* orcid.org/0000-0002-8162-4629; Email: yfmo@umd.edu

Authors

Jianwen Liang − *Department of Mechanical and Materials Engineering, University of Western Ontario, London, Ontario N6A 3K7, Canada*

Xiaona Li − *Department of Mechanical and Materials Engineering, University of Western Ontario, London, Ontario N6A 3K7, Canada*

Shuo Wang − *Department of Materials Science and Engineering, University of Maryland, College Park, Maryland 20742, United States;* orcid.org/0000-0002-7907-9676

Keegan R. Adair − *Department of Mechanical and Materials Engineering, University of Western Ontario, London, Ontario N6A 3K7, Canada*

Weihan Li − *Department of Mechanical and Materials Engineering, University of Western Ontario, London, Ontario N6A 3K7, Canada*

https://dx.doi.org/10.1021/jacs.0c00134
J. Am. Chem. Soc. 2020, 142, 7012–7022

Yang Zhao − *Department of Mechanical and Materials Engineering, University of Western Ontario, London, Ontario N6A 3K7, Canada*
Changhong Wang − *Department of Mechanical and Materials Engineering, University of Western Ontario, London, Ontario N6A 3K7, Canada*
Yongfeng Hu − *Canadian Light Source, Saskatoon, SK S7N 2V3, Canada*
Li Zhang − *China Automotive Battery Research Institute Co. Ltd, Beijing 100088, China*
Shangqian Zhao − *China Automotive Battery Research Institute Co. Ltd, Beijing 100088, China*
Shigang Lu − *China Automotive Battery Research Institute Co. Ltd, Beijing 100088, China*
Huan Huang − *Glabat Solid-State Battery Inc., London, ON N6G 4X8, Canada*
Ruying Li − *Department of Mechanical and Materials Engineering, University of Western Ontario, London, Ontario N6A 3K7, Canada*

Complete contact information is available at: https://pubs.acs.org/10.1021/jacs.0c00134

Author Contributions

[$]J.L., X.L., and S.W. contributed equally to this work.

Notes

The authors declare no competing financial interest.

■ ACKNOWLEDGMENTS

This research was supported by Natural Sciences and Engineering Research Council of Canada (NSERC), GLABAT Solid-State Battery Inc., China Automotive Battery Research Institute Co. Ltd, Canada Research Chair Program (CRC), Canada Foundation for Innovation (CFI), Ontario Research Fund, the Canada Light Source at University of Saskatchewan (CLS), Canada MITACS fellowships, and University of Western Ontario. Y.M. acknowledges the support from National Science Foundation under award No. 1550423. This research used computational facilities from the University of Maryland supercomputing resources and the Maryland Advanced Research Computing Center (MARCC).

■ REFERENCES

(1) Famprikis, T.; Canepa, P.; Dawson, J. A.; Islam, M. S.; Masquelier, C. Fundamentals of inorganic solid-state electrolytes for batteries. *Nat. Mater.* **2019**, *18*, 1278−1291.
(2) Manthiram, A.; Yu, X.; Wang, S. Lithium battery chemistries enabled by solid-state electrolytes. *Nat. Rev. Mater.* **2017**, *2* (4), 16103.
(3) Yang, Q.; Li, C. Li metal batteries and solid state batteries benefiting from halogen-based strategies. *Energy Stor. Mater.* **2018**, *14*, 100−117.
(4) Kamaya, N.; Homma, K.; Yamakawa, Y.; Hirayama, M.; Kanno, R.; Yonemura, M.; Kamiyama, T.; Kato, Y.; Hama, S.; Kawamoto, K.; Mitsui, A. A lithium superionic conductor. *Nat. Mater.* **2011**, *10*, 682.
(5) Kato, Y.; Hori, S.; Saito, T.; Suzuki, K.; Hirayama, M.; Mitsui, A.; Yonemura, M.; Iba, H.; Kanno, R. High-power all-solid-state batteries using sulfide superionic conductors. *Nat. Energy* **2016**, *1* (4), 16030.
(6) Kraft, M. A.; Ohno, S.; Zinkevich, T.; Koerver, R.; Culver, S. P.; Fuchs, T.; Senyshyn, A.; Indris, S.; Morgan, B. J.; Zeier, W. G. Inducing High Ionic Conductivity in the Lithium Superionic Argyrodites $Li_{6+x}P_{1-x}Ge_xS_5I$ for All-Solid-State Batteries. *J. Am. Chem. Soc.* **2018**, *140* (47), 16330−16339.
(7) Nazar, L.; Adeli, P.; Bazak, J. D.; Park, K.-H.; Kochetkov, I.; Huq, A.; Goward, G. Boosting solid-state diffusivity and conductivity in lithium superionic argyrodites by halide substitution. *Angew. Chem., Int. Ed.* **2019**, *58* (26), 8681−8686.
(8) Zhou, L.; Assoud, A.; Zhang, Q.; Wu, X.; Nazar, L. F. A New Family of Argyrodite Thioantimonate Lithium Superionic Conductors. *J. Am. Chem. Soc.* **2019**, *141* (48), 19002−19013.
(9) Li, X.; Ren, Z.; Norouzi Banis, M.; Deng, S.; Zhao, Y.; Sun, Q.; Wang, C.; Yang, X.; Li, W.; Liang, J. Unravelling the Chemistry and Microstructure Evolution of a Cathodic Interface in Sulfide-Based All-Solid-State Li-Ion Batteries. *ACS Energy Lett.* **2019**, *4* (10), 2480−2488.
(10) Ohta, S.; Kobayashi, T.; Asaoka, T. High lithium ionic conductivity in the garnet-type oxide $Li_{7-X}La_3(Zr_{2-X}, Nb_X)O_{12}$ (X= 0−2). *J. Power Sources* **2011**, *196* (6), 3342−3345.
(11) Cuan, J.; Zhou, Y.; Zhou, T.; Ling, S.; Rui, K.; Guo, Z.; Liu, H.; Yu, X. Borohydride-Scaffolded Li/Na/Mg Fast Ionic Conductors for Promising Solid-State Electrolytes. *Adv. Mater.* **2019**, *31* (1), 1803533.
(12) Asano, T.; Sakai, A.; Ouchi, S.; Sakaida, M.; Miyazaki, A.; Hasegawa, S. Solid Halide Electrolytes with High Lithium-Ion Conductivity for Application in 4 V Class Bulk-Type All-Solid-State Batteries. *Adv. Mater.* **2018**, *30* (44), 1803075.
(13) Li, X.; Liang, J.; Luo, J.; Norouzi Banis, M.; Wang, C.; Li, W.; Deng, S.; Yu, C.; Zhao, F.; Hu, Y.; Sham, T.-K.; Zhang, L.; Zhao, S.; Lu, S.; Huang, H.; Li, R.; Adair, K. R.; Sun, X. Air-stable Li_3InCl_6 electrolyte with high voltage compatibility for all-solid-state batteries. *Energy Environ. Sci.* **2019**, *12* (9), 2665−2671.
(14) Li, X.; Liang, J.; Chen, N.; Luo, J.; Adair, K. R.; Wang, C.; Banis, M. N.; Sham, T.-K.; Zhang, L.; Zhao, S.; Lu, S.; Huang, H.; Li, R.; Sun, X. Water-Mediated Synthesis of a Superionic Halide Solid Electrolyte. *Angew. Chem., Int. Ed.* **2019**, *58* (46), 16427−16432.
(15) Hu, J.; Chen, K.; Li, C. Nanostructured Li-rich fluoride coated by ionic liquid as high ion-conductivity solid electrolyte additive to suppress dendrite growth at Li metal anode. *ACS Appl. Mater. Interfaces* **2018**, *10* (40), 34322−34331.
(16) Wang, S.; Bai, Q.; Nolan, A. M.; Liu, Y.; Gong, S.; Sun, Q.; Mo, Y. Lithium Chlorides and Bromides as Promising Solid-State Chemistries for Fast Ion Conductors with Good Electrochemical Stability. *Angew. Chem., Int. Ed.* **2019**, *58* (24), 8039−8043.
(17) Xu, Z.; Chen, X.; Liu, K.; Chen, R.; Zeng, X.; Zhu, H. Influence of anion charge on Li ion diffusion in a new solid-state electrolyte, Li_3LaI_6. *Chem. Mater.* **2019**, *31* (18), 7425−7433.
(18) Feinauer, M.; Euchner, H.; Fichtner, M.; Anji Reddy, M. Unlocking the Potential of Fluoride-based Solid Electrolytes for Solid-State Lithium Batteries. *ACS Appl. Energy Mater.* **2019**, *2* (10), 7196−7203.
(19) Tomita, Y.; Fuji-i, A.; Ohki, H.; Yamada, K.; Okuda, T. New lithium ion conductor Li_3InBr_6 studied by ^{7}Li NMR. *Chem. Lett.* **1998**, *27* (3), 223−224.
(20) Yamada, K.; Kumano, K.; Okuda, T. Lithium superionic conductors Li_3InBr_6 and $LiInBr_4$ studied by ^{7}Li, ^{115}In NMR. *Solid State Ionics* **2006**, *177* (19−25), 1691−1695.
(21) Muy, S.; Voss, J.; Schlem, R.; Koerver, R.; Sedlmaier, S. J.; Maglia, F.; Lamp, P.; Zeier, W. G.; Shao-Horn, Y. High-throughput screening of solid-state Li-ion conductors using lattice-dynamics descriptors. *iScience* **2019**, *16*, 270−282.
(22) Schlem, R.; Muy, S.; Prinz, N.; Banik, A.; Shao-Horn, Y.; Zobel, M.; Zeier, W. G. Mechanochemical Synthesis: A Tool to Tune Cation Site Disorder and Ionic Transport Properties of Li_3MCl_6 (M = Y, Er) Superionic Conductors. *Adv. Energy Mater.* **2020**, *10*, 1903719.
(23) Bohnsack, A.; Balzer, G.; Güdel, H.-U.; Wickleder, M. S.; Meyer, G. Ternäre Halogenide vom Typ A_3MX_6. VII [1]. Die Bromide Li_3MBr_6 (M = Sm-Lu, Y): Synthese, Kristallstruktur, Ionenbeweglichkeit. *Z. Anorg. Allg. Chem.* **1997**, *623* (9), 1352−1356.
(24) Bohnsack, A.; Stenzel, F.; Zajonc, A.; Balzer, G.; Wickleder, M. S.; Meyer, G. Ternäre Halogenide vom Typ A_3MX_6. VI [1]. Ternäre Chloride der Selten-Erd-Elemente mit Lithium, Li_3MCl_6 (M= Tb-Lu, Y, Sc): Synthese, Kristallstrukturen und Ionenbewegung. *Z. Anorg. Allg. Chem.* **1997**, *623* (7), 1067−1073.

(25) Altorfer, F. *Investigations into the fast ionic conductors γ-CuBr, Li_2S, Na_2S, Ba_2NH, $NaTaN_2$ and Li_3HoCl_6 by means of neutron scattering*; Eidgenoessische Technische Hochschule: 1994, LNS−171.
(26) Villars, P.; Cenzual, K.; Daams, J.; Gladyshevskii, R.; Shcherban, O.; Dubenskyy, V.; Melnichenko-Koblyuk, N.; Pavlyuk, O.; Savysyuk, I.; Stoyko, S.; Sysa, L., Li_3ErCl_6. In *Structure Types. Part 6: Space Groups (166) R-3m - (160) R3m*, Villars, P.; Cenzual, K., Eds. Springer Berlin Heidelberg: Berlin, Heidelberg, 2008, 424−424.
(27) Meyer, G.; Wickleder, M. S. Simple and complex halides. *Handbook on the Physics and Chemistry of Rare Earths* **2000**, *28*, 53−129.
(28) Kanno, R.; Takeda, Y.; Yamamoto, O.; Cros, C.; Gang, W.; Hagenmuller, P. Phase transition of the solid lithium ion conductor with the spinel structure: $Li_{2-2x}M_{1+x}Cl_4$ (M= Mg, Mn). *Solid State Ionics* **1986**, *20* (2), 99−103.
(29) Kanno, R.; Takeda, Y.; Takada, K.; Yamamoto, O. Phase diagram and ionic conductivity of the lithium chloride-iron (II) chloride system. *Solid State Ionics* **1983**, *9*, 153−156.
(30) Zissi, G. D.; Papatheodorou, G. N. Composition and temperature induced changes on the structure of molten $ScCl_3$−CsCl mixtures. *Phys. Chem. Chem. Phys.* **2004**, *6* (18), 4480−4489.
(31) Zissi, G. D.; Papatheodorou, G. N. Seven-coordinated scandium (iii) chloroions in $ScCl_3$−CsCl molten mixtures at 600−900° C. *J. Chem. Soc., Dalton Trans.* **2002**, No. 13, 2599−2600.
(32) Kresse, G.; Furthmüller, J. Efficient iterative schemes for ab initio total-energy calculations using a plane-wave basis set. *Phys. Rev. B: Condens. Matter Mater. Phys.* **1996**, *54* (16), 11169.
(33) Blöchl, P. E. Projector augmented-wave method. *Phys. Rev. B: Condens. Matter Mater. Phys.* **1994**, *50* (24), 17953.
(34) Heyd, J.; Scuseria, G. E. Efficient hybrid density functional calculations in solids: Assessment of the Heyd−Scuseria−Ernzerhof screened Coulomb hybrid functional. *J. Chem. Phys.* **2004**, *121* (3), 1187−1192.
(35) Jain, A.; Ong, S. P.; Hautier, G.; Chen, W.; Richards, W. D.; Dacek, S.; Cholia, S.; Gunter, D.; Skinner, D.; Ceder, G. Commentary: The Materials Project: A materials genome approach to accelerating materials innovation. *APL Mater.* **2013**, *1* (1), 011002.
(36) Ong, S. P.; Richards, W. D.; Jain, A.; Hautier, G.; Kocher, M.; Cholia, S.; Gunter, D.; Chevrier, V. L.; Persson, K. A.; Ceder, G. Python Materials Genomics (pymatgen): A robust, open-source python library for materials analysis. *Comput. Mater. Sci.* **2013**, *68*, 314−319.
(37) He, X.; Mo, Y. Accelerated materials design of $Na_{0.5}Bi_{0.5}TiO_3$ oxygen ionic conductors based on first principles calculations. *Phys. Chem. Chem. Phys.* **2015**, *17* (27), 18035−18044.
(38) Bai, Q.; He, X.; Zhu, Y.; Mo, Y. First-principles study of oxyhydride H−ion conductors: toward facile anion conduction in oxide-based materials. *ACS Appl. Energy Mater.* **2018**, *1* (4), 1626−1634.
(39) He, X.; Bai, Q.; Liu, Y.; Nolan, A. M.; Ling, C.; Mo, Y. Crystal Structural Framework of Lithium Super-Ionic Conductors. *Adv. Energy Mater.* **2019**, *9* (43), 1902078.
(40) Zhu, Y.; He, X.; Mo, Y. Origin of outstanding stability in the lithium solid electrolyte materials: insights from thermodynamic analyses based on first-principles calculations. *ACS Appl. Mater. Interfaces* **2015**, *7* (42), 23685−23693.
(41) Zhu, Y.; He, X.; Mo, Y. Strategies based on nitride materials chemistry to stabilize Li metal anode. *Adv. Sci.* **2017**, *4* (8), 1600517.
(42) Zhu, Y.; He, X.; Mo, Y. First principles study on electrochemical and chemical stability of solid electrolyte−electrode interfaces in all-solid-state Li-ion batteries. *J. Mater. Chem. A* **2016**, *4* (9), 3253−3266.
(43) Nolan, A. M.; Zhu, Y.; He, X.; Bai, Q.; Mo, Y. Computation-Accelerated Design of Materials and Interfaces for All-Solid-State Lithium-Ion Batteries. *Joule* **2018**, *2* (10), 2016−2046.
(44) Emly, A.; Kioupakis, E.; Van der Ven, A. Phase stability and transport mechanisms in antiperovskite Li_3OCl and Li_3OBr superionic conductors. *Chem. Mater.* **2013**, *25* (23), 4663−4670.
(45) Han, F.; Gao, T.; Zhu, Y.; Gaskell, K. J.; Wang, C. A Battery Made from a Single Material. *Adv. Mater.* **2015**, *27* (23), 3473−3483.
(46) Tan, D. H.; Wu, E. A.; Nguyen, H.; Chen, Z.; Marple, M. A.; Doux, J.-M.; Wang, X.; Yang, H.; Banerjee, A.; Meng, Y. S. Elucidating Reversible Electrochemical Redox of Li_6PS_5Cl Solid Electrolyte. *ACS Energy Lett.* **2019**, *4*, 2418−2427.
(47) Dewald, G. F.; Ohno, S.; Kraft, M. A.; Koerver, R.; Till, P.; Vargas-Barbosa, N. M.; Janek, J.; Zeier, W. G. Experimental Assessment of the Practical Oxidative Stability of Lithium Thiophosphate Solid Electrolytes. *Chem. Mater.* **2019**, *31* (20), 8328−8337.
(48) Chassé, M.; Juhin, A.; Cabaret, D.; Delhommaye, S.; Vantelon, D.; Calas, G. Influence of crystallographic environment on scandium K-edge X-ray absorption near-edge structure spectra. *Phys. Chem. Chem. Phys.* **2018**, *20* (37), 23903−23912.
(49) Lindqvist-Reis, P.; Persson, I.; Sandström, M. The hydration of the scandium (III) ion in aqueous solution and crystalline hydrates studied by XAFS spectroscopy, large-angle X-ray scattering and crystallography. *Dalton Trans.* **2006**, No. 32, 3868−3878.
(50) Löble, M. W.; Keith, J. M.; Altman, A. B.; Stieber, S. C. E.; Batista, E. R.; Boland, K. S.; Conradson, S. D.; Clark, D. L.; Lezama Pacheco, J.; Kozimor, S. A. Covalency in Lanthanides. An X-ray Absorption Spectroscopy and Density Functional Theory Study of $LnCl_6^{x-}$(x= 3, 2). *J. Am. Chem. Soc.* **2015**, *137* (7), 2506−2523.

https://dx.doi.org/10.1021/jacs.0c00134
J. Am. Chem. Soc. 2020, 142, 7012−7022